Structure of the turnip yellows virus particles. How is the readthrough domain exposed on the capsid surface?

Joséphine Lai-Kee-Him [a], Stefano Trapani [b,*], Sylvaine Boissinot [c,1], Catherine Reinbold [d], Chloé Fallet [e], Aurélie Ancelin [f], François Lecorre [g], François Hoh [h], Véronique Ziegler-Graff [i], Véronique Brault [j,*] and Patrick Bron [k,*]

[a] Centre de Biologie Structurale (CBS), Univ Montpellier, CNRS, INSERM, Montpellier, France; josephine.laikeehim@cbs.cnrs.fr

[b] Centre de Biologie Structurale (CBS), Univ Montpellier, CNRS, INSERM, Montpellier, France; stefano.trapani@umontpellier.fr

[c] INRAE, Université de Strasbourg, UMR SVQV, Colmar France; sylvaine.boissinot@inrae.fr

[d] INRAE, Université de Strasbourg, UMR SVQV, Colmar France; catherine.reinbold@inrae.fr

[e] Centre de Biologie Structurale (CBS), Univ Montpellier, CNRS, INSERM, Montpellier, France.

[f] Centre de Biologie Structurale (CBS), Univ Montpellier, CNRS, INSERM, Montpellier, France; aurelie.ancelin@cbs.cnrs.fr

[g] Centre de Biologie Structurale (CBS), Univ Montpellier, CNRS, INSERM, Montpellier, France.

[h] Centre de Biologie Structurale (CBS), Univ Montpellier, CNRS, INSERM, Montpellier, France; francois.hoh@cnrs.fr

[i] Institut de biologie moléculaire des plantes, CNRS, Université de Strasbourg, Strasbourg, France; veronique.ziegler-graff@ibmp-cnrs.unistra.fr

[j] INRAE, Université de Strasbourg, UMR SVQV, Colmar France; veronique.brault@inrae.fr

[k] Centre de Biologie Structurale (CBS), Univ Montpellier, CNRS, INSERM, Montpellier, France; patrick.bron@cbs.cnrs.fr

[1] Current address: INRAE, BFP UMR 1332, Villenave d'Ornon, France

[*] Corresponding authors

Abstract: The polerovirus turnip yellows virus (TuYV) (formerly beet western yellows virus, BWYV) is a member of the genus *Polerovirus* in the family *Solemoviridae*. It is transmitted from plant to plant by aphids according to a circulative and non-propagative mode. TuYV has a wide host range among herbaceous plants and infects important crops such as oilseed rape. Members of the *Solemoviridae* family are strictly restricted to the three cell types constituting the phloem; the nucleated phloem parenchyma cells and companion cells, where the virus replicates, and the sieve elements, which convey the virus to sites distant from the inoculation point. TuYV consists of a single-stranded positive sense RNA genome of approximately 6 kb encapsidated into an icosahedral capsid of approximately 30 nm in diameter. The capsid is composed of two types of subunits: the major capsid protein (CP, ~23 kDa) and a minor component, denoted RTP* (~54 kDa), which arises from the C-terminal cleavage of a readthrough gene product (RTP, 74 kDa). The minor capsid component contains the CP sequence at its N-terminus fused with a structured domain (denoted ^{N}RTD) which has been shown to be a key determinant of virus transmission and necessary for crossing aphid gut epithelial cells during viral uptake. Though both the CP and RTP* structural proteins are involved in virus movement and aphid transmission, how RTP* is incorporated in the viral particles is poorly understood. We present here the structural characterisation of the TuYV wild-type virions (viral capsids containing both CP and RPT*) and a mutant whose capsids contain the CP only. The comparison of the cryo-EM maps of the wild-type and the mutated virus (resolved at 4.1 and 3.5 Å respectively) reveals that the RTP* does not impair the structural organization of the capsid shell. Furthermore, electron cryo-microscopy and immunogold labelling observations of both viruses indicate that the ^{N}RTDs do not adopt well-defined positions relative to the capsid surface, and that only four to six ^{N}RTDs or ^{N}RTD dimers are incorporated into the viral particles, suggesting a random insertion of the RTP* into the TuYV capsid.

Keywords: polerovirus, readthrough domain, capsid, elevated dodecahedron, structure, electron cryo-microscopy, immunogold labelling

Introduction

Turnip yellows virus (TuYV) (formerly beet western yellows virus) is a member of the genus *Polerovirus*. Members of the genera *Polerovirus* and *Enamovirus* (family *Solemoviridae*) and *Luteovirus* (family *Tombusviridae*), hereafter referred to as P/E/L viruses, are important plant pathogens that affect many major crops (Heck and Brault, 2018). Their economic importance extends worldwide to small grains, potato, brassicas, cotton, cucurbits, pepper, sugarcane and sorghum. P/E/L viruses are phloem-restricted and transmitted exclusively by aphids in nature (Gildow, 1999). The P/E/L genome is a linear single-stranded positive-sense RNA with an intricate organization of the open reading frames (ORFs) (Smirnova et al., 2015; Sõmera et al., 2021) (Fig. 1a). The genome is encapsidated into a non-enveloped particle of ~30 nm in diameter composed of 180 subunits arranged according to a *T*=3 icosahedral symmetry. Most of the 180 subunits are the major capsid protein (CP) of about 22-25 kDa encoded by ORF3. However, some of the subunits (10 to 25%) contain a C-terminal extension which protrudes at the virion surface (Brault et al., 1995; Filichkin et al., 1994). This minor capsid protein (hereafter called RTP*, ~55 kDa) arises from stochastic translational readthrough of the CP stop codon, whereby a non-structural readthrough protein (RTP) of about 74 kDa is produced (Fig. 1b). The RTP contains the CP sequence on the N-ter side, followed by a proline-rich flexible linker and a readthrough domain (RTD). This is composed of a structured sub-domain (denoted ^{N}RTD) (Schiltz et al., 2022) and a C-ter sub-domain (denoted ^{C}RTD) which is predicted to be intrinsically disordered (LaTourrette et al., 2021). Post-translational cleavage of the ^{C}RTD stretch from the RTP results in the structural RTP* which is incorporated in the capsids (Fig. 1b).

The role of RTP, RTP* and CP in P/E/L virus movement and transmission by aphids has been extensively addressed, based mainly on reverse genetics on TuYV, potato leafroll virus (PLRV, species *Polerovirus PLRV*), barley yellow dwarf virus (BYDV, species *Polerovirus WYDVGPV*) and cucurbit aphid-borne yellows virus (CABYV, species *Polerovirus CABYV*). The full-length non-structural RTP is involved in virus systemic invasion of the plant (Boissinot et al., 2014; Brault et al., 1995; Hipper et al., 2014; Kaplan et al., 2007; Lee et al., 2005; Mutterer et al., 1999; Peter et al., 2008; Rodriguez-Medina et al., 2015; Wang et al., 1995; Xu et al., 2018) and the terminal ^{C}RTD plays a role in restricting PLRV to the phloem (Peter et al., 2009) and in symptom development (Bruyère et al., 1997; Rodriguez-Medina et al., 2015). The presence of both CP and RTP* in intact virions is required for the virus to move long distance within host plants and for transmission by aphid vectors (Brault et al., 1995; Chay et al., 1996; Hipper et al., 2014; Lee et al., 2005). It has been shown that both TuYV structural proteins interact with the ephrin receptor, an aphid protein involved in virus uptake and transmission (Mulot et al., 2018). Also, the ^{N}RTD of RTP* has been identified as a key determinant of transmission as mutant viruses devoid of the whole RTD are not aphid transmissible and retain the ability to infect plants only at a reduced titre (Brault et al., 1995; Chay et al., 1996; Liang et al., 2004; Reutenauer et al., 1993). Conversely, mutants lacking just the ^{C}RTD assemble efficiently into virions (Boissinot et al., 2014; Bruyère et al., 1997), retain the ability to interact with aphid proteins (Mulot et al., 2018) and can be transmitted to new hosts (Wang et al., 1995).

In vitro and *in vivo* binding assays also revealed that TuYV and PLRV virions bind to plant components (Bencharki et al., 2010; DeBlasio et al., 2016, 2015a, 2015b).

The structure of P/E/L capsids and how they interact with aphid vectors have been the object of investigation for several years. Difficulties in producing enough purified viruses had long limited structural studies to homology modelling coupled to mutational and cross-linking experiments (Alexander et al., 2017; Brault et al., 2003; Chavez et al., 2012; Kaplan et al., 2007; Terradot et al., 2001; Torrance, 1992). Significant advances were made after the production of BYDV and PLRV virus-like particles (VLPs) containing the recombinant CP, but not the RTP*, and the establishment of their atomic structure by electron cryogenic microscopy (cryo-EM) (Byrne et al., 2019). Also, the crystal structure of the ^{N}RTD (absent from the VLPs) was solved using recombinant forms of the isolated domains from PLRV and TuYV (Schiltz et al., 2022). These studies revealed that P/E/L viruses are structurally related to picorna-like viruses, corrected errors in previously proposed structural models, and rationalized the observations from previous mutagenesis studies. The ^{N}RTD structure revealed a dimeric architecture in which the sequence of each monomer goes back and forth from a jell-roll domain to a cap domain. The ^{N}RTD jelly roll was found to be structurally related to the constitutively expressed capsid protrusions (P domains) of tombusviruses, while the cap domain is absent from those viruses. A model, based on the tombusvirus structure, of how the ^{N}RTD might be presented on the surface of P/E/L viruses was proposed (Schiltz et al., 2022).

To understand if and how the presence of the RTP* affects the P/E/L capsid structure and how the ^{N}RTD is presented on the capsid surface, we have purified and studied two forms of TuYV particles: the wild-type virus (TuYV-WT, viral capsids containing both CP and RPT*) and a mutant (TuYV-ΔRTP) whose capsids contain the CP only. The two forms have been observed and characterised by electron microscopy (EM) techniques (negative staining, immunogold labelling, 3D cryo-EM). In this paper we present and discuss the results of our observations.

Materials and Methods

Virus production and purification

Purified virions were prepared from 320 g of frozen leaf material of *N. benthamiana* infiltrated with TuYV-WT full-length infectious clone using agroinfiltration (English et al., 1997) and from 335 g of *Montia perfoliata* similarly infiltrated with TuYV-ΔRTP full-length clone (Leiser et al., 1992). Infiltrated leaves were collected and frozen at –80 °C 6 to 8 days post-inoculation. The purification was performed according to van den Heuvel et al. (1991) and completed by a sucrose density gradient centrifugation followed by ultracentrifugation at 45 000 rpm during 2 h 30 min at 17 °C to obtain a highly concentrated suspension of virions. The final pellet was suspended in citrate buffer 0.1 M pH 6.0 and stored at –80 °C. The final concentration reached 1.32 µg/µL and 3.5 µg/µL for TuYV-WT and TuYV-ΔRTP respectively.

Immunogold labelling of viruses

Formvar/carbon coated 300 mesh nickel grids were allowed to float for 30 min on drops of purified TuYV-WT or TuYV-ΔRTP at about 100 ng/µL in citrate buffer 0.1 M

(pH 6.0). Grids were then incubated in blocking buffer (PBS + 2% BSA) for 30 min and transferred to drops containing purified immunoglobulins at 0.8 mg/mL directed against the TuYV RTD (dilution 1:40 in PBS) (Reutenauer et al., 1993). Incubation was conducted overnight at 4 °C. Grids were rinsed in blocking buffer (30 min) and incubated in goat anti-rabbit IgG conjugated with 10 nm gold beads for 3 h 30 min (1:20 in PBS 0.1% BSA) (BBInternational, Cardiff, UK). Grids were rinsed with PBS then with water and finally stained with 3% uranyl acetate. Grids were observed with a Philips EM 208 transmission electron microscope operating at 80 kV.

Negative stain electron microscopy

Negative stain EM grids were prepared by applying 3 µL virus solution to collodion-carbon coated copper grids for 2 min. The excess of liquid was blotted with Whatman N4 filter paper and the grids were washed twice in 1% (w/v) uranyl acetate for 1 min. The excess liquid was removed, and grids were air-dried. The grids were observed using a JEOL 2200 FS electron microscope operating at 200 kV in zero-energy-loss mode with a slit width of 20 eV and equipped with a 4k × 4k slow-scan CDD camera (Gatan inc.)

Cryo-EM

Preliminary images were recorded using a JEOL 2200 FS electron microscope operating at 200 kV in zero-energy-loss mode with a slit width of 20 eV and equipped with a 4k × 4k slow-scan CDD camera (Gatan inc.). We initially prepared frozen-hydrated viruses deposited onto Quantifoil R2/2 or R1.2/1.3 grids (Quantifoil Micro tools GmbH, Germany) or glow discharged Lacey grid (Ted Pella Inc., USA), blotted for 3 s and then flash frozen in liquid ethane using the semi-automated plunge freezing device Vitrobot IV at 100% relative humidity. Observations revealed that even at high nominal concentrations (up to 3.5 mg/mL) the final concentration of viruses within the grid holes was not enough for an automatic image acquisition. Indeed, most of the virus particles interacted with the carbon film and TuYV-ΔRTP also formed nanocrystals. To overcome this problem, we used Quantifoil R2/2 grids covered with a 10-15 nm carbon film, which led to virus concentrations suitable for a single-particle cryo-EM analysis. No deformation of viral particles was observed, indicating that they were apparently not impaired by the interaction with the carbon film.

For high-resolution data collection, 3 µL of purified viral particles at ~1 mg/mL were applied during 2 min to glow-discharged Quantifoil R 2/2 grids covered with a thin carbon film (Quantifoil Micro tools GmbH, Germany), blotted for 3 s and then flash frozen in liquid ethane using the semi-automated plunge freezing device Vitrobot IV at 100% relative humidity. A Polara transmission electron microscope (Thermo Fisher Scientific, Eindhoven, Netherlands) (IBS, Grenoble, France) was used operating at 300 kV with defocus ranging from –0.8 to –2.5 µm. The pixel size estimated at the specimen level was 0.97 Å. A total of 151 and 179 movies were recorded for TuYV-WT and TuYV-ΔRTP respectively, using the Gatan Latitude single particle acquisition software (Gatan inc.) on a K2 camera in counting mode. The total exposure time was 5 s corresponding to a dose of 50 $e^-/Å^2$. Forty individual frames were collected with an electron dose of 1.0 $e^-/Å^2$ per frame.

Image processing and 3D reconstructions

Image processing was carried out using RELION 3.1 for icosahedral reconstructions, RELION 4.0 for focussed asymmetric classifications, Gctf (Zhang, 2016) for contrast transfer function (CTF) calculations, Gautomatch (developed by Kai Zhang at the MRC Laboratory of Molecular Biology, UK) for automatic particle picking, and Blocres from the Bsoft package (Heymann, 2001) for local resolution estimation.

The frames of each movie were computationally corrected for drift and beam-induced movement (Zivanov et al., 2018) and the CTF calculated. 51 930 TuYV-WT and 26 519 TuYV-ΔRTP particles were automatically picked, extracted from the movies and rescaled (pixel size: 2.91 Å, box size: 160 pixels) and submitted to reference-free 2D classification with regularisation parameter τ=2 and mask diameter=377 Å. 40 780 TuYV-WT and 18 433 TuYV-ΔRTP particles were selected from the best 2D classes and used to compute *de novo* 3D models at 15 Å resolution. Icosahedral symmetry was imposed during the model computation. Further particles were discarded based on the results of 3D classifications (pixel size: 1.22526 Å, box size: 380 pixels, τ: 4, mask diameter: 375 Å, number of classes: 4) and 3D alignment refinements with icosahedral symmetry constraints. The sets of particles producing the best reconstructions were used for per-particle defocus refinement and Bayesian polishing. Ultimately, 17 316 TuYV-WT and 12 174 TuYV-ΔRTP selected particles yielded icosahedral reconstructions at 4.1 Å and 3.5 Å resolution respectively (resolution estimation based on a 0.143 gold-standard FSC threshold on masked maps (Chen et al., 2013; Scheres and Chen, 2012)). The refined maps were post-processed through model masking and *B*-factor sharpening ($B = -137$ Å^2 and –60.5 Å^2 for TuYV-WT and TuYV-ΔRTP respectively).

To reconstruct the ^{N}RTD from the TuYV-WT images, several asymmetric 3D classifications were run focussed on one twofold axis of the CP shell. An I_2 and a Q_2 axis were independently targeted (see Results for the definition of these symbols). A hemispherical search region was defined around the targeted axis, the height and base of the hemisphere lying, respectively, on the symmetry axis and just underneath the capsid surface. The radius of the hemisphere (180 Å) was chosen to largely encompass a hypothetical ^{N}RTD dimer (PDB 7uln was used as a reference) connected to the CP shell through extended linkers (21 residues/linker in polyproline helix conformation). The set of 17 316 aligned images of the TuYV-WT particles was symmetry-expanded (x60). Projections of the TuYV-WT reconstructed capsid were subtracted from the images of the expanded set, except for a small region of the protein shell (corresponding approximately to the volume of four CP monomers) surrounding the twofold axis. The subtracted images were recentred at the base of the hemispherical search region and re-boxed (box size: 312 pixels, pixel size: 1.22526 Å). Several masks of varying shapes and sizes were defined within the hemispherical search region. With each mask, extensive 3D classifications were carried out without symmetry constraints (τ: 4-10-20-40-60, number of classes: 4, mask diameter: 300-360 Å). However, all attempts to isolate and reconstruct the ^{N}RTD were unsuccessful.

Atomic model building, refinement and analysis

A preliminary atomic model of the TuYV-ΔRTP capsid was set up by rigid-body fitting the secondary structure core of PDB entry 2FZ1 (species *Tymovirus brassicae*, formerly *Turnip yellow mosaic virus*) into the cryo-EM density map (note that the structures of other polerovirus capsids were not yet available in the PDB in 2019 when this work was carried out). The amino acid sequence assignment was guided by secondary structure predictions and the density of several bulky side chains visible in the map. Loops were reconstructed using *Coot* (Emsley et al., 2010). This preliminary model was iteratively refined against the experimental density map – following the general guidelines described by Afonine et al. (2018a) – by alternated steps of automatic refinement under stereochemical restraints with PHENIX.real_space_refine (Afonine et al., 2018b), visual model inspection and correction with *Coot* and model geometry validation with MolProbity (Williams et al., 2018). To save computation time and memory and, at the same time, correctly avoid steric clashes between symmetry related neighbouring chains, only a part of the whole T=3 icosahedral capsid density was considered, which consisted of seventeen subunits (two hexamers and a pentamer, see the description of the structure in Results). During refinement, tight non-crystallographic symmetry (NCS) restraints were applied to maintain equivalent and quasi-equivalent chains in the same conformation. NCS restraints were released towards the end of the refinement for those residues sitting at quasi-equivalent subunit interfaces. Standard stereochemical restraints and manually tuned secondary-structure restraints were applied during all refinement steps. Atomic isotropic displacement parameters (one parameter per residue) were applied and refined in the final steps.

The TuYV-WT atomic structure was similarly refined using the TuYV-ΔRTP structure as a starting point.

Subunit-subunit interfaces were analysed using PISA (Krissinel and Henrick, 2007).

The directions and positions of the local symmetry axes in the final structures were calculated by least-squares optimisation (under matrix-orthogonality constraints) of the group of matrices associated to an exact n-fold axis with respect to the transformations obtained by pair-wise alignment of the relevant subunits.

Artwork

Figures were prepared using: UCSF Chimera (Pettersen et al., 2004), developed by the Resource for Biocomputing, Visualization, and Informatics at the University of California, San Francisco, with support from NIH P41-GM103311; UCSF ChimeraX (Meng et al., 2023), developed by the Resource for Biocomputing, Visualization, and Informatics at the University of California, San Francisco, with support from National Institutes of Health R01-GM129325 and the Office of Cyber Infrastructure and Computational Biology, National Institute of Allergy and Infectious Diseases; PyMOL open source, version 2.5.0 (Schrödinger, LLC, 2024).

Results

Characterization of purified viral particles by negative staining and immunogold labelling

TuYV virions were purified by sucrose density centrifugation from agroinfiltrated leaves of plants inoculated with the wild-type (TuYV-WT) or a mutant clone (TuYV-ΔRTP)

265 devoid of RTP* (Fig. 1). The mutant (called BWYV-6.4 in Brault et al. (1995)) is affected in
266 plant systemic infection and is not transmissible by aphids (Brault et al., 1995). TuYV-ΔRTP
267 virions are supposed to be composed solely of CP subunits whereas the wild-type virions
268 should contain both CP and RTP* (Fig. 1).
269 Observation of negatively stained TuYV-WT virions by transmission EM revealed
270 circular particles with a diameter of approximately 30 nm (Fig. 2a). In the TuYV-ΔRTP
271 samples two particle shapes are reproducibly observed: circular, sized as the wild-type
272 virions (Fig. 2d), and slightly elongated (Fig. 2e). This latter shape has never been observed
273 in preparations of purified TuYV-WT. TuYV-ΔRTP particles were rather smooth (Fig. 2d),
274 while TuYV-WT virions displayed protruding densities at their surface (indicated by black
275 arrows in Fig. 2a), likely the ^{N}RTD from the RTP*.
276 Immunogold labelling experiments using antibodies directed against the RTD
277 (Reutenauer et al., 1993) confirm exposition of the ^{N}RTD at the surface of the TuYV-WT
278 virions (Fig. 2b-c) as previously shown on virions partially purified from TuYV-infected
279 plant protoplasts (Brault et al., 1995). No gold labelling was observed on TuYV-ΔRTP
280 virions (Figure 2f). We estimated that the number of gold beads per viral particles in the EM
281 images (Table S1) varies from 0 to 3 or 4. This is consistent with the presence of the
282 protrusions observed in negatively stained samples.
283 We found that TuYV-ΔRTP can form large 2D-arrays of particles in negatively stained
284 samples (Fig. 3a) and also small 3D crystals in frozen hydrated samples at a concentration
285 of 3.5 mg/mL (Fig. 3b) as already seen in aphids fed on purified TuYV-ΔRTP (Reinbold et
286 al., 2001). The regularity of these assemblies seems to be interrupted by the incorporation
287 of elongated particles (black arrows in Fig. 3a). This extensive regular organization has
288 never been observed for the wild-type virions neither by negative stain nor by cryo-EM.
289 Only some assemblies of 2 or 4 virions were observed in negatively stained samples (Fig.
290 3c). This different behaviour suggests that the presence of RTP* in TuYV-WT strongly
291 impairs the interplay between viral particles.

292 *Cryo-EM 3D reconstruction of TuYV-WT and TuYV-ΔRTP*

293 Frozen-hydrated samples of TuYV-WT and TuYV-ΔRTP were prepared on Quantifoil
294 R2/2 grids (holey carbon) covered with a carbon film to avoid preferential aggregation at
295 the hole borders and formation of nanocrystals (as illustrated in Fig. 3b). Transmission EM
296 images of the samples were collected using a Polara microscope equipped with a K2
297 camera. In most of the images, uniform distributions of mostly undistorted, RNA-filled
298 spherical virions were observed (Fig. 4a). The 3D scattering densities of the TuYV-WT and
299 TuYV-ΔRTP virions were reconstructed from selected sets of, respectively, 17 316 and
300 3 003 homogeneous, RNA-filled particles (Fig. 4b-c). The overall resolution of the
301 reconstructed maps (refined by imposing icosahedral symmetry constraints) is estimated
302 (according to the 0.143 gold-standard FSC criterion) at 4.1 Å (TuYV-WT) and 3.5 Å
303 (TuYV-ΔRTP). Both the protein shell (which is well resolved in the sharpened maps, Fig.
304 4b) and the RNA shell (uninterpretable due to icosahedral averaging) are visible in the
305 unsharpened, unmasked maps (Fig. 4c). Atomic models of the capsids, comprising more
306 than two thirds of the length of the CP domains (from residue 62/64 to residue 202), have
307 been built and refined against the reconstructed densities (Fig. 4d-h). No interpretable
308 density could be attributed to the long arginine-rich N-terminal stretches (Fig. 4h), which

are predicted to be disordered and likely buried in the nucleic acid at the interior of the virions. Expectedly, due to symmetry averaging during the reconstruction procedure, no extra density indicative of the presence of the ^{N}RTD shows up in the TuYV-WT reconstruction (asymmetric reconstructions are discussed later). The atomic models of the CP assemblies do not reveal any significant difference between the TuYV-WT and TuYV-ΔRTP protein shells (Fig. 4e). Direct comparison of the trimers in the icosahedral asymmetric unit (without rigid-body adjustments of their positions) shows a low root mean square deviation (RMSD) between main-chain atoms (0.32 Å). Rigid body fit of individual subunit pairs results in slight improvements of the RMSD (0.22-0.25 Å), but with negligible movements of the subunits (0.2-1.0° rotations).

The CP architeture

If not otherwise stated, the terms "chain" and "subunit" in this subsection will refer to the visible (modelled) part of the CP domains in the TuYV capsid structures (unframed sequences in Fig. 4h). Though we report calculated values (e.g. RMSD, rotation angles) for the TuYV-ΔRTP structure only, all the considerations that follow are valid for both TuYV-WT and TuYV-ΔRTP.

The TuYV capsid is composed by 180 copies of the CP domain arranged according to icosahedral rotational symmetry with triangulation number T=3. One icosahedral asymmetric unit comprises three quasi-equivalent subunits (chains A, B and C in Fig. 5a) related by an almost exact, local threefold axis (denoted Q_3, Fig. 5a-b). Each subunit folds into a classical jelly roll (Fig. 4g), commonly found in viruses, composed of two packed four-stranded anti-parallel β-sheets. In TuYV, one of the β-sheets faces the interior of the capsid while the other faces the exterior. Two intervening α-helices, most of the loops, the N- and C-ter β-strands and a few residues from other strands of the jelly roll provide interactions between subunits (Fig. 4g).

The geometry of the overall assembly can be described in terms of an equilateral elevated dodecahedron (EED, Fig. 5c). This is a non-convex polyhedron composed of sixty equilateral triangular faces, where each face represents, with respect to the icosahedral symmetry of the assembly, one asymmetric unit. The sixty faces of the EED, grouped by five around the twelve fivefold axes, can be thought of as the faces of pentagonal pyramids whose bases sit on the faces of an underlying regular dodecahedron (outlined by blue edges in Fig. 5c). The dihedral angles between triangular faces sharing a common edge are convex towards either the capsid interior or the capsid exterior, so that two dihedral angle values (named *endo* and *exo*, respectively) and two classes of edges (named accordingly) can be defined (Fig. 5c). The actual TuYV geometry is quite close to that of an ideal EED. The values of the *endo* and *exo* angles (141° and 174° respectively), evaluated by comparing the directions of the TuYV Q_3 axes, are close to the ideal values (138.19° and 168.68° respectively) (Fig. 5f-g). The virtual hinge movement that would transform an *exo* into an *endo* interface corresponds to a rotation of ~45° in TuYV as compared to 53.13° in an ideal EED.

Besides the global icosahedral symmetry, the EED arrangement implies a set of local symmetry axes. Fig. 5d (see also Fig. S1) illustrates how the EED global and local symmetry can be derived by virtually folding an ideal 2D hexagonal lattice according to the *endo* and *exo* angles. We will use the symbols I_n, (n = 2, 3, 5) and Q_n (n = 2, 3, 5, 6) to

denote, respectively, global (icosahedral) and local (quasi) *n*-fold symmetry. The approximate positions of the I_n and Q_n axes are indicated in Fig. 5e. The TuYV capsid can be formally described as an assembly of pentamers and hexamers centred on the I_5 and I_3 icosahedral axes respectively. Fig. 5e shows a set of two hexamers (chains $BC_2B_3C_4B_5C_6$ and $CB_2C_3B_4C_5B_6$) and one pentamer (chains $AA_2A_3A_4A_5$). This portion of the capsid encompasses one asymmetric unit plus all its adjacent subunits. Pentamers obey strict fivefold symmetry. Hexamers obey threefold but not sixfold symmetry and are composed of two sets of interleaved subunits (blue and green subunits respectively in Fig. 5h) not related by icosahedral symmetry. Large deviations from ideal sixfold symmetry are observed around the I_3 axes. Superposition of adjacent chains within a hexamer requires either a quasi-sixfold (Q_6) rotation of 60.1° or a quasi-fivefold (Q_5) rotation of 67.4° around axes that are not collinear with the I_3 axis. The Q_6-I_3 and Q_5-I_3 axes misalignments are 23.0° and 20.6° respectively (Fig. 5i). Note that Q_5 rotations give rise to an arrangement of adjacent subunits (ex. subunits CB_2 in Fig. 5e,h,i) similar to that observed within pentamers (ex. subunits AA_2 in Fig. 5e), hence the preferred symbol Q_5 (instead of Q_6). Also, non-equivalent triplets of subunits can be found (e.g. ABA_2 and CAB_2) which are arranged essentially in the same way and whose local symmetry axes would be compatible with those of a T=1 icosahedron (Fig. 5j, Fig. 6). This is a consequence of pentamers and hexamers sharing *endo* angles (Fig. 5e).

A total of eight independent —*i.e.* not related by icosahedral symmetry— interfaces between subunits exist. We have labelled the interfaces according to the rotation (I_n or Q_n) relating the contacting subunits (Table 1). The portion of capsid illustrated in Fig. 5e contains at least one representative of the eight interfaces. Interacting residues at the subunit interfaces are mainly of a polar or charged nature (Table 2, Fig. 6). No major differences are observed among the three Q_3 interfaces (though these are not strictly equivalent in principle) nor between the Q_5 and I_5 interfaces. (Table 2, Fig. 6). On the other hand, significant differences are found at the I_2 (when compared to Q_2) and Q_6 (when compared to Q_5 or I_5) interfaces. These differences are related to the existence, in an EED, of different dihedral angles: the Q_2, Q_5 and I_5 interfaces are found on *endo* edges, while the I_2 and Q_6 interfaces are found on *exo* edges. Indeed, most residues involved in Q_5, I_5, Q_6, Q_2 and I_2 interfaces line the edges of the EED (Fig. 6). The virtual hinge movement transforming an *endo* interface into an *exo* interface (Fig. 5g) would occur around a line of atomic contacts between helices α1 of neighbouring subunits. This transformation maintains the two helices in close contact but disrupts interactions and separate the underlying N-ter and C-ter β-sheets in adjacent chains (Fig. 6). The cryo-EM maps indicate that the increased space available under the α1-helices at the I_2 interfaces is not occupied by an additionally ordered stretch of polypeptide chain.

The unreconstructed ^{N}RTD is likely to float at the capsid exterior

Inspection of some selected cryo-EM images confirmed the presence of the ^{N}RTD (four to six protrusions of the capsid) in the purified TuYV-WT samples (Fig. 7a), but its scattering density was not visible in the cryo-EM map of the capsid due to the symmetry averaging. We tried to reconstruct this domain by applying asymmetric classification and reconstruction procedures. As the ^{N}RTD has been reported to form homodimers (Schiltz et al., 2022), we focussed our search mainly within hemispherical regions (whose size

accounted also for the length of the CP- ^{N}RTD linker) surrounding an I_2 or Q_2 axis in proximity of the capsid (Fig. 7b). Despite our extensive attempts (see Materials and Methods), we could not obtain any convincing result. We propose, thus, that the ^{N}RTD does not occupy well-defined positions on the capsid surface.

Discussion

The structure of the TuYV capsid shows no significant differences with the previously published structures of polerovirus VLPs (Byrne et al., 2019) (RMSD 0.7 Å in comparison with PLRV and BYDV VLPs). More generally, the *T*=3 subunit arrangement of TuYV follows the scheme initially described by Rossmann et al. (1983a) for southern bean mosaic virus (SBMV, species *Sobemovirus SBMV*), in which the quasi-equivalence of contacts (Caspar and Klug, 1962) is assured essentially by different relative orientations of the subunits at the Q_2 and I_2 interfaces (dimeric interfaces) where the α1-helices touch each other. Differently to what happens in SBMV, the cryo-EM maps of TuYV indicate that the increased space available under the α1-helices at the I_2 interfaces is not occupied by an additionally ordered stretch of polypeptide chain.

We have described the TuYV assembly in terms of an equilateral elevated dodecahedron (EED), within the framework of Caspar and Klug's theory on the principles governing regular virus structures (Caspar and Klug, 1962) (but see Brinkmann et al. (2017), Janner (2006), Twarock (2006) and Twarock & Luque (2019) for different and more general theoretical approaches). The EED geometrical model can be applied, to different degrees of approximation, to many (but not all) viruses with *T*=3 icosahedral symmetry. TuYV shows small deviations from this ideal geometry (Fig. 5g,i). We have analysed all virus structures classified as *T*=3 in the VIPERdb (Montiel-Garcia et al., 2021) and found that, among those that can be reconducted to the EED geometry, a very limited number strictly adhere to that model (ex. panicum mosaic virus, species *Panicovirus panici*), while most of the others, like tomato bushy stunt virus (TBSV, species *Tombusvirus lycopersici*) and SBMV, deviate to some extent (imperfect Q_3 rotations within the asymmetric unit). Other geometrical descriptions have been used in the past for some of these viruses. TBSV and SBMV have been described as rhombic triacontahedra (Alexander et al., 2017; Johnson and Olson, 2021; Rossmann et al., 1983b), polyhedra composed by non-equilateral triangles forming, in pairs, flat rhombic faces (*exo* angle = 180°). The polerovirus PLRV has also been described as possessing flat *exo* angles (Adams et al., 2022), but by comparing it with TuYV we propose that PLRV also has non-flat *exo* interfaces. Other *T*=3 icosahedral viruses (like brome mosaic virus, species *Bromovirus BMV*) cannot be described by the EED model, but rather by a regular icosahedron obtained by folding a 2D hexagonal lattice (as described by Caspar and Klug (1962) in their seminal paper) along *endo* edges only, thus resulting in a different set of local symmetries (Fig. S1). We could also point out that, while the EED geometry was not explicitly cited by Caspar and Klug, they indeed included a papercraft picture of an EED, and not an icosahedron, in Fig. 8c of their paper to illustrate the *T*=3 architecture.

We demonstrated, by immunogold labelling, that the TuYV-WT virions we purified contain (a variable number of) the ^{N}RTD extensions. These protrusions of the capsid were visible in the negatively stained samples and in some cryo-EM images. Schiltz et al. (2022) showed that, *in vitro*, the ^{N}RTD forms dimers structurally related to the dimeric P domains

that protrude along the I_2 and Q_2 axes of the capsids of TBSV and other tombusviruses. Based on the TuYV-ΔRTP structure described in this paper (released by the PDB in July 2022), and by comparison with TBSV, Schiltz et al. (2022) showed that, in principle, it is structurally possible for the ^{N}RTD dimers to be accommodated (like in TBSV) in tight contact with the TuYV CP layer and even occupy the complete set of 90 twofold sites on the capsid surface. Failure of our extensive attempts to reconstruct the ^{N}RTD around the twofold sites suggests, however, that the ^{N}RTD domain does not occupy (in the conditions of our purified samples) a well-defined position on the capsid surface. Indeed, the proline-rich linker (21 residues) connecting the CP and ^{N}RTD domain in TuYV is much longer than the stretch (7 residues) joining the TBSV P domain to the capsid shell, and this may allow the ^{N}RTD to float around (at least in absence of a specific interacting partner) in proximity of the capsid surface.

We have seen no significant differences between the cryo-EM maps of TuYV-WT and TuYV-ΔRTP, indicating that the presence of the ^{N}RTD domains did not influence the final CP fold and assembly organisation (of the selected particles). One cannot exclude, however, the possibility of ^{N}RTD playing a role in RNA packaging and capsid assembly (formation of elongated particles has been observed in TuYV-ΔRTP but not in TuYV-WT samples).

The varying number of beads per virion observed after immunogold labelling suggests a lack of accessibility of some ^{N}RTDs, or a heterogeneous population of viruses incorporating a different number of RTP* subunits, or different RTP* conformations, some of which would not be recognised by the antibodies. This raises the question whether different forms exist of the ^{N}RTD at the surface of the capsid that may have different cellular partners and fulfil different functions in the virus cycle. Answers to these questions will require further investigation.

Deposited data references

The cryo-EM maps of TuYV-WT and TuYV-ΔRTP have been deposited with the Electron Microscopy Data Bank and released under the accession IDs EMD-10003 and EMD-10001 respectively. The model atomic coordinates have been deposited with the Protein Data Bank and released under the PDB IDs 9fhp and 6rtk respectively.

Funding sources

This work was funded by the French Infrastructure for Integrated Structural Biology (FRISBI), grant ANR-10-INSB-05.

References

Adams, M.C., Schiltz, C.J., Heck, M.L., Chappie, J.S., 2022. Crystal structure of the potato leafroll virus coat protein and implications for viral assembly. Journal of Structural Biology 214, 107811. https://doi.org/10.1016/j.jsb.2021.107811

Afonine, P.V., Klaholz, B.P., Moriarty, N.W., Poon, B.K., Sobolev, O.V., Terwilliger, T.C., Adams, P.D., Urzhumtsev, A., 2018a. New tools for the analysis and validation of cryo-EM maps and atomic models. Acta Cryst D 74, 814–840. https://doi.org/10.1107/S2059798318009324

Afonine, P.V., Poon, B.K., Read, R.J., Sobolev, O.V., Terwilliger, T.C., Urzhumtsev, A., Adams, P.D., 2018b. Real-space refinement in PHENIX for cryo-EM and crystallography. Acta Cryst D 74, 531–544. https://doi.org/10.1107/S2059798318006551

Alexander, M.M., Mohr, J.P., DeBlasio, S.L., Chavez, J.D., Ziegler-Graff, V., Brault, V., Bruce, J.E., Heck, M. (Cilia), 2017. Insights in luteovirid structural biology guided by chemical cross-linking and high resolution mass spectrometry. Virus Research, Plant Virus Epidemiology 241, 42–52. https://doi.org/10.1016/j.virusres.2017.05.005

Bencharki, B., Boissinot, S., Revollon, S., Ziegler-Graff, V., Erdinger, M., Wiss, L., Dinant, S., Renard, D., Beuve, M., Lemaitre-Guillier, C., Brault, V., 2010. Phloem Protein Partners of Cucurbit aphid borne yellows virus: Possible Involvement of Phloem Proteins in Virus Transmission by Aphids. MPMI 23, 799–810. https://doi.org/10.1094/MPMI-23-6-0799

Boissinot, S., Erdinger, M., Monsion, B., Ziegler-Graff, V., Brault, V., 2014. Both Structural and Non-Structural Forms of the Readthrough Protein of Cucurbit aphid-borne yellows virus Are Essential for Efficient Systemic Infection of Plants. PLOS ONE 9, e93448. https://doi.org/10.1371/journal.pone.0093448

Brault, V., Bergdoll, M., Mutterer, J., Prasad, V., Pfeffer, S., Erdinger, M., Richards, K.E., Ziegler-Graff, V., 2003. Effects of Point Mutations in the Major Capsid Protein of Beet Western Yellows Virus on Capsid Formation, Virus Accumulation, and Aphid Transmission. J Virol 77, 3247–3256. https://doi.org/10.1128/JVI.77.5.3247-3256.2003

Brault, V., van den Heuvel, J.F., Verbeek, M., Ziegler-Graff, V., Reutenauer, A., Herrbach, E., Garaud, J.C., Guilley, H., Richards, K., Jonard, G., 1995. Aphid transmission of beet western yellows luteovirus requires the minor capsid read-through protein P74. The EMBO Journal 14, 650–659. https://doi.org/10.1002/j.1460-2075.1995.tb07043.x

Brinkmann, G., Goetschalckx, P., Schein, S., 2017. Comparing the constructions of Goldberg, Fuller, Caspar, Klug and Coxeter, and a general approach to local symmetry-preserving operations. Proceedings of the Royal Society A: Mathematical, Physical and Engineering Sciences 473, 20170267. https://doi.org/10.1098/rspa.2017.0267

Bruyère, A., Brault, V., Ziegler-Graff, V., Simonis, M.-T., Van den Heuvel, J.F.J.M., Richards, K., Guilley, H., Jonard, G., Herrbach, E., 1997. Effects of Mutations in the Beet Western Yellows Virus Readthrough Protein on Its Expression and Packaging and on Virus Accumulation, Symptoms, and Aphid Transmission. Virology 230, 323–334. https://doi.org/10.1006/viro.1997.8476

Byrne, M.J., Steele, J.F.C., Hesketh, E.L., Walden, M., Thompson, R.F., Lomonossoff, G.P., Ranson, N.A., 2019. Combining Transient Expression and Cryo-EM to Obtain High-Resolution Structures of Luteovirid Particles. Structure 27, 1761-1770.e3. https://doi.org/10.1016/j.str.2019.09.010

Caspar, D.L., Klug, A., 1962. Physical principles in the construction of regular viruses. Cold Spring Harb. Symp. Quant. Biol. 27, 1–24.

Chavez, J.D., Cilia, M., Weisbrod, C.R., Ju, H.-J., Eng, J.K., Gray, S.M., Bruce, J.E., 2012. Cross-linking Measurements of the Potato leafroll virus Reveal Protein Interaction Topologies Required for Virion Stability, Aphid Transmission, and Virus–Plant Interactions. J. Proteome Res. 11, 2968–2981. https://doi.org/10.1021/pr300041t

Chay, C.A., Gunasinge, U.B., Dinesh-kumar, S.P., Miller, W.A., Gray, S.M., 1996. Aphid Transmission and Systemic Plant Infection Determinants of Barley Yellow Dwarf Luteovirus-PAV are Contained in the Coat Protein Readthrough Domain and 17-kDa Protein, Respectively. Virology 219, 57–65. https://doi.org/10.1006/viro.1996.0222

Chen, S., McMullan, G., Faruqi, A.R., Murshudov, G.N., Short, J.M., Scheres, S.H.W., Henderson, R., 2013. High-resolution noise substitution to measure overfitting and validate resolution in 3D structure determination by single particle electron cryomicroscopy. Ultramicroscopy 135, 24–35. https://doi.org/10.1016/j.ultramic.2013.06.004

DeBlasio, S.L., Chavez, J.D., Alexander, M.M., Ramsey, J., Eng, J.K., Mahoney, J., Gray, S.M., Bruce, J.E., Cilia, M., 2016. Visualization of Host-Polerovirus Interaction Topologies Using Protein Interaction Reporter Technology. Journal of Virology 90, 1973–1987. https://doi.org/10.1128/jvi.01706-15

DeBlasio, S.L., Johnson, R., Mahoney, J., Karasev, A., Gray, S.M., MacCoss, M.J., Cilia, M., 2015a. Insights Into the Polerovirus–Plant Interactome Revealed by Coimmunoprecipitation and Mass Spectrometry. MPMI 28, 467–481. https://doi.org/10.1094/MPMI-11-14-0363-R

DeBlasio, S.L., Johnson, R., Sweeney, M.M., Karasev, A., Gray, S.M., MacCoss, M.J., Cilia, M., 2015b. Potato leafroll virus structural proteins manipulate overlapping, yet distinct protein interaction networks during infection. PROTEOMICS 15, 2098–2112. https://doi.org/10.1002/pmic.201400594

Emsley, P., Lohkamp, B., Scott, W.G., Cowtan, K., 2010. Features and development of Coot. Acta Cryst D 66, 486–501. https://doi.org/10.1107/S0907444910007493

English, J.J., Davenport, G.F., Elmayan, T., Vaucheret, H., Baulcombe, D.C., 1997. Requirement of sense transcription for homology-dependent virus resistance and trans-inactivation. The Plant Journal 12, 597–603. https://doi.org/10.1046/j.1365-313X.1997.00597.x

Filichkin, S.A., Lister, R.M., McGrath, P.F., Young, M.J., 1994. *In Vivo* Expression and Mutational Analysis of the Barley Yellow Dwarf Virus Readthrough Gene. Virology 205, 290–299. https://doi.org/10.1006/viro.1994.1645

Gildow, F.E., 1999. Luteovirus transmission and mechanisms regulating vector specificity, in: The Luteoviridae. CABI publishing, Wallingford, pp. 88–113.

Heck, M., Brault, V., 2018. Targeted disruption of aphid transmission: a vision for the management of crop diseases caused by Luteoviridae members. Current Opinion in Virology 33, 24–32. https://doi.org/10.1016/j.coviro.2018.07.007

Heymann, J.B., 2001. Bsoft: Image and Molecular Processing in Electron Microscopy. Journal of Structural Biology 133, 156–169. https://doi.org/10.1006/jsbi.2001.4339

Hipper, C., Monsion, B., Bortolamiol-Bécet, D., Ziegler-Graff, V., Brault, V., 2014. Formation of virions is strictly required for turnip yellows virus long-distance movement in plants. Journal of General Virology 95, 496–505. https://doi.org/10.1099/vir.0.058867-0

J. M. Van Den Heuvel, J.F., 1991. Transmission of Potato Leafroll Virus from Plants and Artificial Diets by *Myzus persicae*. Phytopathology 81, 150. https://doi.org/10.1094/Phyto-81-150

Janner, A., 2006. Towards a classification of icosahedral viruses in terms of indexed polyhedra. Acta Crystallogr A Found Crystallogr 62, 319–330. https://doi.org/10.1107/S0108767306022227

Johnson, J.E., Olson, A.J., 2021. Icosahedral virus structures and the protein data bank. Journal of Biological Chemistry 296. https://doi.org/10.1016/j.jbc.2021.100554

Kaplan, I.B., Lee, L., Ripoll, D.R., Palukaitis, P., Gildow, F., Gray, S.M., 2007. Point mutations in the potato leafroll virus major capsid protein alter virion stability and aphid transmission. Journal of General Virology 88, 1821–1830. https://doi.org/10.1099/vir.0.82837-0

Krissinel, E., Henrick, K., 2007. Inference of Macromolecular Assemblies from Crystalline State. Journal of Molecular Biology 372, 774–797. https://doi.org/10.1016/j.jmb.2007.05.022

LaTourrette, K., Holste, N.M., Garcia-Ruiz, H., 2021. Polerovirus genomic variation. Virus Evolution 7, veab102. https://doi.org/10.1093/ve/veab102

Lee, L., Kaplan, I.B., Ripoll, D.R., Liang, D., Palukaitis, P., Gray, S.M., 2005. A Surface Loop of the Potato Leafroll Virus Coat Protein Is Involved in Virion Assembly, Systemic Movement, and Aphid Transmission. Journal of Virology 79, 1207–1214. https://doi.org/10.1128/jvi.79.2.1207-1214.2005

Leiser, R.M., Ziegler-Graff, V., Reutenauer, A., Herrbach, E., Lemaire, O., Guilley, H., Richards, K., Jonard, G., 1992. Agroinfection as an alternative to insects for infecting plants with beet western yellows luteovirus. Proceedings of the National Academy of Sciences 89, 9136–9140. https://doi.org/10.1073/pnas.89.19.9136

577 Liang, D., Gray, S.M., Kaplan, I., Palukaitis, P., 2004. Site-Directed Mutagenesis and Generation of Chimeric
578 Viruses by Homologous Recombination in Yeast to Facilitate Analysis of Plant-Virus Interactions. MPMI
579 17, 571–576. https://doi.org/10.1094/MPMI.2004.17.6.571

580 Meng, E.C., Goddard, T.D., Pettersen, E.F., Couch, G.S., Pearson, Z.J., Morris, J.H., Ferrin, T.E., 2023.
581 UCSF CHIMERAX : Tools for structure building and analysis. Protein Science 32, e4792.
582 https://doi.org/10.1002/pro.4792

583 Montiel-Garcia, D., Santoyo-Rivera, N., Ho, P., Carrillo-Tripp, M., III, C.L.B., Johnson, J.E., Reddy, V.S.,
584 2021. VIPERdb v3.0: a structure-based data analytics platform for viral capsids. Nucleic Acids Research
585 49, D809–D816. https://doi.org/10.1093/nar/gkaa1096

586 Mulot, M., Monsion, B., Boissinot, S., Rastegar, M., Meyer, S., Bochet, N., Brault, V., 2018. Transmission of
587 Turnip yellows virus by Myzus persicae Is Reduced by Feeding Aphids on Double-Stranded RNA
588 Targeting the Ephrin Receptor Protein. Front. Microbiol. 9. https://doi.org/10.3389/fmicb.2018.00457

589 Mutterer, J.D., Stussi-Garaud, C., Michler, P., Richards, K.E., Jonard, G., Ziegler-Graff, V., 1999. Role of the
590 beet western yellows virus readthrough protein in virus movement in Nicotiana clevelandii. Journal of
591 General Virology 80, 2771–2778. https://doi.org/10.1099/0022-1317-80-10-2771

592 Peter, K.A., Gildow, F., Palukaitis, P., Gray, S.M., 2009. The C Terminus of the Polerovirus P5 Readthrough
593 Domain Limits Virus Infection to the Phloem. Journal of Virology 83, 5419–5429.
594 https://doi.org/10.1128/jvi.02312-08

595 Peter, K.A., Liang, D., Palukaitis, P., Gray, S.M., 2008. Small deletions in the potato leafroll virus
596 readthrough protein affect particle morphology, aphid transmission, virus movement and accumulation.
597 Journal of General Virology 89, 2037–2045. https://doi.org/10.1099/vir.0.83625-0

598 Pettersen, E.F., Goddard, T.D., Huang, C.C., Couch, G.S., Greenblatt, D.M., Meng, E.C., Ferrin, T.E., 2004.
599 UCSF Chimera—A visualization system for exploratory research and analysis. Journal of Computational
600 Chemistry 25, 1605–1612. https://doi.org/10.1002/jcc.20084

601 Reinbold, C., Gildow, F.E., Herrbach, E., Ziegler-Graff, V., Gonçalves, M.C., van den Heuvel, J.F.J.M.,
602 Brault, V., 2001. Studies on the role of the minor capsid protein in transport of Beet western yellows virus
603 through Myzus persicae. Journal of General Virology 82, 1995–2007.
604 https://doi.org/10.1099/0022-1317-82-8-1995

605 Reutenauer, A., Ziegler-Graff, V., Lot, H., Scheidecker, D., Guilley, H., Richards, K., Jonard, G., 1993.
606 Identification of Beet Western Yellows Luteovirus Genes Implicated in Viral Replication and Particle
607 Morphogenesis. Virology 195, 692–699. https://doi.org/10.1006/viro.1993.1420

608 Rodriguez-Medina, C., Boissinot, S., Chapuis, S., Gereige, D., Rastegar, M., Erdinger, M., Revers, F.,
609 Ziegler-Graff, V., Brault, V., 2015. A protein kinase binds the C-terminal domain of the readthrough
610 protein of *Turnip yellows virus* and regulates virus accumulation. Virology 486, 44–53.
611 https://doi.org/10.1016/j.virol.2015.08.031

612 Rossmann, M.G., Abad-Zapatero, C., Hermodson, M.A., Erickson, J.W., Huber, R., 1983a. Subunit
613 interactions in southern bean mosaic virus. Journal of Molecular Biology 166, 37–73.
614 https://doi.org/10.1016/S0022-2836(83)80049-7

615 Rossmann, M.G., Abad-Zapatero, C., Murthy, M.R.N., Liljas, L., Jones, T.A., Strandberg, B., 1983b.
616 Structural comparisons of some small spherical plant viruses. Journal of Molecular Biology 165, 711–
617 736. https://doi.org/10.1016/S0022-2836(83)80276-9

618 Scheres, S.H.W., Chen, S., 2012. Prevention of overfitting in cryo-EM structure determination. Nature
619 Methods 9, 853–854. https://doi.org/10.1038/nmeth.2115

620 Schiltz, C.J., Wilson, J.R., Hosford, C.J., Adams, M.C., Preising, S.E., DeBlasio, S.L., MacLeod, H.J., Van
621 Eck, J., Heck, M.L., Chappie, J.S., 2022. Polerovirus N-terminal readthrough domain structures reveal
622 molecular strategies for mitigating virus transmission by aphids. Nat Commun 13, 6368.
623 https://doi.org/10.1038/s41467-022-33979-2

624 Schrödinger, LLC, 2024. The PyMOL Molecular Graphics System, Version 2.5.0.

625 Smirnova, E., Firth, A.E., Miller, W.A., Scheidecker, D., Brault, V., Reinbold, C., Rakotondrafara, A.M.,
626 Chung, B.Y.-W., Ziegler-Graff, V., 2015. Discovery of a Small Non-AUG-Initiated ORF in Poleroviruses
627 and Luteoviruses That Is Required for Long-Distance Movement. PLOS Pathogens 11, e1004868.
628 https://doi.org/10.1371/journal.ppat.1004868

Sõmera, M., Fargette, D., Hébrard, E., Sarmiento, C., ICTV Report Consortium, 2021. ICTV Virus Taxonomy Profile: Solemoviridae 2021. Journal of General Virology 102, 001707. https://doi.org/10.1099/jgv.0.001707

Terradot, L., Souchet, M., Tran, V., Giblot Ducray-Bourdin, D., 2001. Analysis of a Three-Dimensional Structure of *Potato leafroll virus* Coat Protein Obtained by Homology Modeling. Virology 286, 72–82. https://doi.org/10.1006/viro.2001.0900

Torrance, L., 1992. Analysis of epitopes on potato leafroll virus capsid protein. Virology 191, 485–489. https://doi.org/10.1016/0042-6822(92)90216-C

Twarock, R., 2006. Mathematical virology: a novel approach to the structure and assembly of viruses. Phil. Trans. R. Soc. A. 364, 3357–3373. https://doi.org/10.1098/rsta.2006.1900

Twarock, R., Luque, A., 2019. Structural puzzles in virology solved with an overarching icosahedral design principle. Nat Commun 10, 4414. https://doi.org/10.1038/s41467-019-12367-3

Wang, J.Y., Chay, C., Gildow, F.E., Gray, S.M., 1995. Readthrough Protein Associated with Virions of Barley Yellow Dwarf Luteovirus and Its Potential Role in Regulating the Efficiency of Aphid Transmission. Virology 206, 954–962. https://doi.org/10.1006/viro.1995.1018

Williams, C.J., Headd, J.J., Moriarty, N.W., Prisant, M.G., Videau, L.L., Deis, L.N., Verma, V., Keedy, D.A., Hintze, B.J., Chen, V.B., Jain, S., Lewis, S.M., Arendall, W.B., Snoeyink, J., Adams, P.D., Lovell, S.C., Richardson, J.S., Richardson, D.C., 2018. MolProbity: More and better reference data for improved all-atom structure validation. Protein Science 27, 293–315. https://doi.org/10.1002/pro.3330

Xu, Y., Silva, W.L.D., Qian, Y., Gray, S.M., 2018. An aromatic amino acid and associated helix in the C-terminus of the potato leafroll virus minor capsid protein regulate systemic infection and symptom expression. PLOS Pathogens 14, e1007451. https://doi.org/10.1371/journal.ppat.1007451

Zhang, K., 2016. Gctf: Real-time CTF determination and correction. Journal of Structural Biology 193, 1–12. https://doi.org/10.1016/j.jsb.2015.11.003

Zivanov, J., Nakane, T., Forsberg, B.O., Kimanius, D., Hagen, W.J., Lindahl, E., Scheres, S.H., 2018. New tools for automated high-resolution cryo-EM structure determination in RELION-3. eLife 7, e42166. https://doi.org/10.7554/eLife.42166

Tables

Superposed chains [(a)]	AB	CA	$BC \approx B_6C_2$	$A_2B \approx AB_2$	CC_2	$A_2A \approx AA_5$	$B_2C \approx BC_6$	$CB_6 \approx C_3B_2 \approx C_2B$
C^{α} RMSD	0.59 Å	0.58 Å	0.61 Å	0.59 Å	0.00 Å	0.00 Å	0.61 Å	0.61 Å
Rotation angle	120.23°	119.97°	119.97°	178.76°	180.00°	72.00°	67.39°	60.09°
Translation amplitude	0.53 Å	0.33 Å	0.21 Å	1.38 Å	0.00 Å	0.00 Å	0.46 Å	0.74 Å
Rotation label	Q_3	Q_3	Q_3	Q_2	I_2	I_5	Q_5 [(b)]	Q_6 [(b)]

[(a)] Chain labels as in Fig. 5e. The "≈" symbol indicates equivalent interactions according to icosahedral symmetry.
[(b)] Note that Q_6 and Q_5 compose an I_3 rotation: $Q_6 \cdot Q_5 = I_3$.

Table 1. Geometric relationships between interacting subunits.
Results of pairwise rigid-body superposition of interacting subunits found within one asymmetric unit and its neighbourhoods. Chains are labelled as in Fig. 5e.

Subunit pairs [§]	Residues from the first subunit	Residues from the second subunit
AB (Q_3) BC (Q_3) CA (Q_3)	$E_{129}LDPH_{133}$, $K_{135}L_{136}$, $S_{140}S_{141}$, I_{143} , $S_{159}Y_{160}$, N_{162} , E_{165}	$H_{103}E_{104}$, $E_{165}WHD_{168}$, $H_{199}NPK_{202}$
B_2C (Q_5) A_2A (I_5)	V_{68} , S_{70} , D_{72} , I_{186} , S_{189} , R_{191} , $V_{115}SEASSQ_{121}$	$S_{120}QNSGS_{125}$, $T_{142}INK_{145}$, K_{150}
CB_6 (Q_6)	$D_{72}N_{73}$, $S_{185}I_{186}$, $E_{117}ASSQN_{122}$	$S_{120}QSGS_{125}$, $T_{142}I_{143}$, K_{145} , N_{181}
A_2B (Q_2)	$S_{64}ETFV_{68}$, $P_{92}A_{93}$, $N_{96}G_{97}$, $K_{100}AY_{102}$, F_{198} , $P_{201}K_{202}$	$S_{64}ETFV_{68}$, $P_{92}A_{93}$, $N_{96}G_{97}$, $K_{100}AY_{102}$, F_{198} , $P_{201}K_{202}$
CC_2 (I_2)	$P_{92}A_{93}$, $N_{96}G_{97}$, $K_{100}A_{101}$	$P_{92}A_{93}$, $N_{96}G_{97}$, $K_{100}A_{101}$

§ Chains and rotation axis labelled as in Fig. 5e

Table 2. Residues at the interfaces between subunits.

Figure captions

Fig. 1. Encoding and organisation of the structural proteins in TuYV.

(**a**) TuYV genome organisation. The numbered rectangles represent ORFs. The VPg capping is indicated at the genome 5' end. (**b**) Schematic representation of a wild-type virion (TuYV-WT). The capsid is composed of a mixture of the major coat protein (CP) and the minor coat protein (RTP*). An (arbitrary) number of ^{N}RTD extensions (from the RTP*) are represented by small spheres. (**c**) Representation of the ORF3 and 5 in the wild-type virus and their expression products (RTP, RTP* and CP). The readthrough position at the ORF3 stop codon, the putative cleavage site on the RTP and the proline-rich linker are indicated by triangles. (**d**) Schematic representation of the TuYV-ΔRTP mutant, whose capsid is composed exclusively of the major coat protein. (**e**) as in (**c**) for the TuYV-ΔRTP mutant. The deletion of the ORF5 sequence is indicated by a dotted line.

Fig. 2. EM images of negatively stained and immunogold-labelled TuYV samples.

(**a**) Negatively stained wild-type virions. Protrusions of the capsid (probable presence of the RTP*) are indicated by arrows. (**b**-**c**) Immunogold-labelled wild-type virions. Gold particles (darker spots) indicate the presence of the RTP*. (**d**) Negatively stained mutated virions. No clear protrusion of the capsid is observed. (**e**) Elongated particles observed in samples of the mutant. (**f**) Mutated virions after immunogold labelling. No gold particle is observed, indicative of the absence of the RTP*. Scale bar in panels b, c and f is 100 nm.

Fig. 3. TuYV-ΔRTP assembles into nanocrystals, while TuYV-WT does not.

(**a**) Two-dimensional array of negatively stained TuYV-ΔRTP virions. Arrows indicate elongated or distorted particles. (**b**) Cryo-EM image of TuYV-ΔRTP particles arranged in small, thin 3D crystals. (**c**) Negatively stained TuYV-WT virions forming small assemblies of 2 to 4 particles.

Fig. 4. Cryo-EM reconstruction of TuYV-WT and TuYV-ΔRTP

(**a**) Motion-corrected EM images of frozen-hydrated virions deposited on Quantifoil R2/2 grids covered with a carbon film. Scale bar is 100 nm. Images are low-pass filtered at 15 Å for illustration purposes. (**b**) 3D scattering-density (sharpened maps) of the TuYV virions reconstructed by imposing icosahedral symmetry. Three protein subunits, composing one asymmetric unit of the assembly, are highlighted in colours (blue, magenta, green). The underlying geometry of the assembly (equilateral elevated dodecahedron) is represented by coloured (blue and magenta) edges. The EMDB accession codes are reported. (**c**) Sectional view of the unsharpened, unmasked maps, illustrating the outer (protein) and inner (RNA) layers. The density is coloured according to the distance from the centre of the particle. (**d**) Atomic models of the capsid protein layers. (**e**) Comparison of the TuYV-WT and TuYV-ΔRTP atomic models. The icosahedral asymmetric units (trimers) are shown superposed on to each other and coloured by per-residue RMSD. (**f**) Ribbon representation of the atomic model of one of the CP subunits fitted in the cryo-EM map. (**g**) Two views of the atomic model of one of the CP subunits. Secondary structure elements are labelled. Residues involved in inter-subunit contacts are coloured orange. (**h**) Sequence of the three quasi-equivalent CP domains. Unmodelled regions (no interpretable density) are within red frames. Secondary structure elements are highlighted and labelled as in (g).

Fig. 5 Architecture of the TuYV capsid.

(**a**) Top view from the capsid exterior (left) and side view (right) of one asymmetric unit of the icosahedral assembly. The three subunits (chains A, B and C) are pairwise related by almost exact threefold axes (yellow rods). An ideal threefold axis (calculated by a least-squares fitting procedure) is indicated by a blue vertical rod and labelled Q_3. (**b**) Two views of the three subunits superposed onto each other and oriented as chain C in (a). The ideal threefold axis (Q_3) is shown in blue. The results of pairwise superpositions of the asymmetric unit chains are reported. (**c**) Representation of the equilateral elevated dodecahedron (EED) used for describing the TuYV capsid. The three subunits in one asymmetric unit are also shown. Two pairs of triangular faces, one in *endo* and the other in *exo* configuration, are highlighted in green and orange respectively. *Endo* and *exo* edges are coloured magenta and blue respectively. (**d**) Symmetry diagram of a virtual hexagonal lattice (top) and the resulting EED lattice (bottom) upon folding along the *endo* (magenta) and *exo* (blue) edges. The colours of the symmetry symbols (in the bottom picture) indicate how the nature of the symmetry axes changes upon folding: black means transformation into an icosahedral axis of the same order as in the hexagonal lattice, violet means transformation into an icosahedral axis of a different order, and orange means transformation into a local symmetry axis. (**e**) Arrangement of subunits around one asymmetric unit (viewed from the capsid exterior). Subunits related by an icosahedral rotation are coloured the same and labelled with the same letter, while quasi equivalent subunits not related by icosahedral rotations are coloured differently and labelled with different letters. The approximate positions of icosahedral *n*-fold (I_n, $n = 2, 3, 5$) and local-symmetry quasi *n*-fold (Q_n, $n = 2, 3, 5, 6$) axes are indicated by the yellow labels. The triangle delimits one icosahedral asymmetric unit (*endo* edges in magenta, *exo* edge in blue). (**f**) Two pairs of asymmetric units forming an *exo* (top) or *endo* edge (bottom). On the left: the triangular faces of and ideal EED are also shown. The leftmost faces are orthogonal to the view direction. On the right: the directions perpendicular to the faces of an ideal EED are indicated by the orange or green rods, while the actual local threefold axes of TuYV are indicated by the blue rods. (**g**) An *endo* and an *exo* pairs of asymmetric units represented superposed. The view direction is along the axis of the virtual hinge movement that would transforms an *endo* angle into an *exo* angle. (**h**) Hexameric arrangement of TuYV subunits around an I_3 axis of the ideal EED. Only subunits coloured the same are related by the icosahedral threefold symmetry. EED edges coloured as in (c). (**i**) A portion of a hexamer (three adjacent subunits) and the rotation axes relating pairs of these subunits. The thicker rods (labelled Q_6, I_3 and Q_5) indicate the actual axis directions in the TuYV capsid. The two thinner rods close to the Q_6 and Q_5 axes represent the directions of the corresponding axes in an ideal EED. For reference, the six EED faces underlying a complete hexamer are (partly) visible. (**j**) Two quasi-equivalent triplets of subunits, showing that the quasi-symmetry axes relating their chains would be compatible with those of a T=1 icosahedral assembly.

Fig. 6. The eight non-equivalent subunit interfaces.

In each panel a triplet of subunits surrounding and *exo* or *endo* edge (coloured vertical line) is represented, and the interface between two out of the three subunits (yellow labels) is highlighted. Subunits are labelled as in Fig. 5. Interacting residues are represented in coloured stick mode.

Fig. 7. Observation of capsid protrusions derived from ^{N}RTD on TuYV-WT virions by cryo-EM.

(**a**) Top: cryo-EM images of purified TuYV-WT virions in which some ^{N}RTDs (indicated by arrow) are visible in the proximity of the capsids. Bottom: for comparison, some images of the TuYV-ΔRTP in similar orientations. (**b**) Illustration of the regions surrounding either the I_2 or the Q_2 interfaces that have been targeted for asymmetric reconstructions of the ^{N}RTD. The portion of the cryo-EM density of the capsid used for signal subtraction from the 2D particle images is shown in grey. The asymmetric reconstructions from the full set of pre-aligned signal-subtracted images are shown in colours.

760 **Supplementary data**

761
762
763
764
765
766

Grids	Particles with no gold bead	Particles with one gold bead	Particles with two gold beads	Particles with three or four gold beads	% of labelled particles
TuYV-WT #958	348 (64.4%)	165 (30.6%)	27 (5.0%)	0 (0%)	35.6%
TuYV-WT #968	356 (60.8%)	197 (33.6%)	28 (4.8%)	5 (0.8%)	39.2%
TuYV-WT #960	317 (66.2%)	129 (26.9%)	29 (6.1%)	4 (0.8%)	33.8%
TuYV-WT #959	351 (67.2%)	145 (27.8%)	24 (4.6%)	2 (0.4%)	32.8%
TuYV-WT #966	351 (61.6%)	163 (28.6%)	44 (7.7%)	12 (2.1%)	38.4%
TuYV-ΔRTP #970	393 (99.0%)	4 (1.0%)	0 (0%)	0 (0%)	1.0%
TuYV-ΔRTP #973	470 (99.4%)	2 (0.4%)	1 (0.2%)	0 (0%)	0.4%
TuYV-ΔRTP #972	394 (99.5%)	2 (0.5%)	0 (0%)	0 (0%)	0.5%
TuYV-ΔRTP #974	416 (98.8%)	4 (1.0%)	1 (0.2%)	0 (0%)	1.2%
TuYV-ΔRTP #975	465 (98.9%)	4 (0.9%)	1 (0.2%)	0 (0%)	1.1%

767

768 **Table S1. Estimation of the number of immunogold-labelled TuYV particles.**
769 Estimation of the number of TuYV particles labelled with different numbers of gold beads after incubation
770 with immunoglobulins specifically directed against the TuYV RTD. Observations made on 10 samples
771 (grids), 5 containing the wild-type and 5 containing the mutated TuYV-ΔRTP virus.

772

a

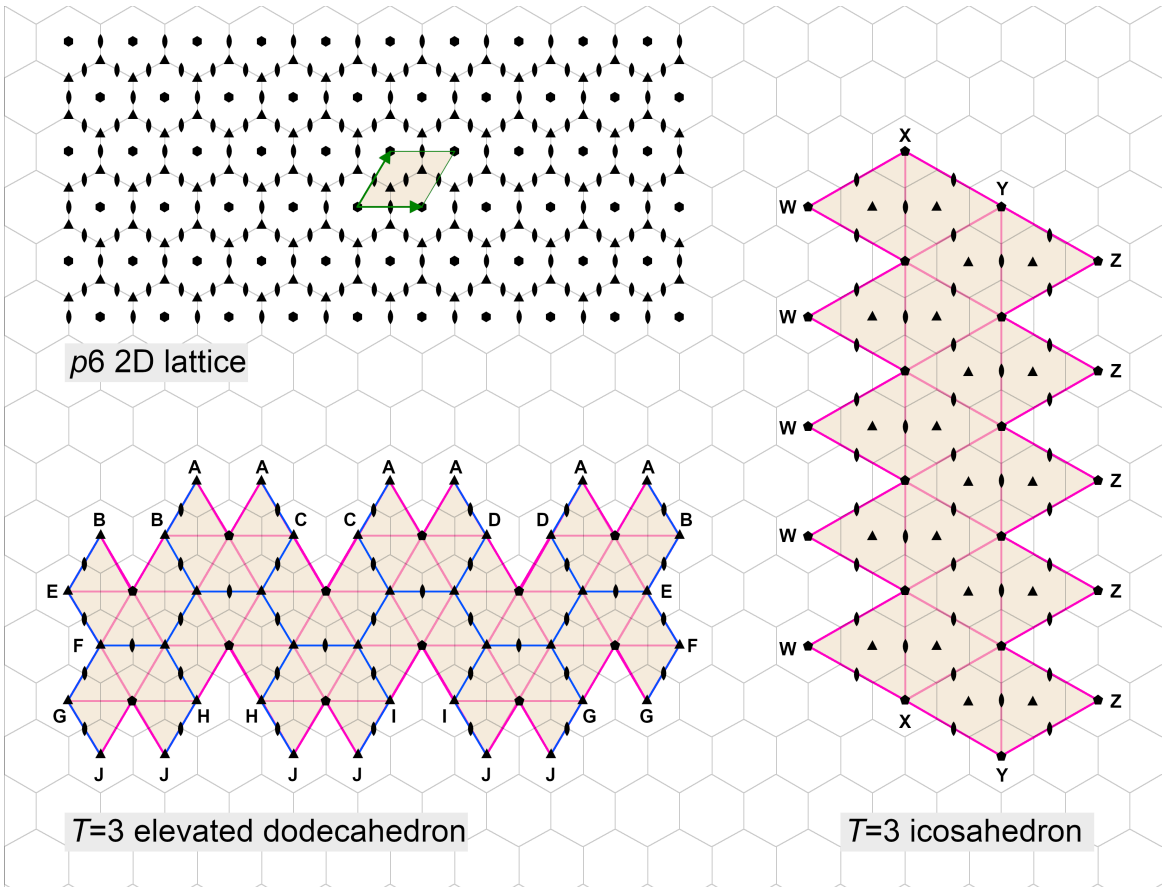

b

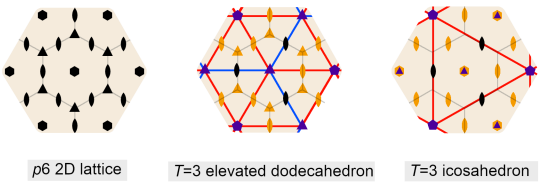

Fig. S1. Folding of a hexagonal lattice into either an icosahedron or an elevated dodecahedron.

(**a**) Folding of a 2D hexagonal lattice (plane space group *p*6) into a *T*=3 icosahedron or a *T*=3 equilateral elevated dodecahedron (EED). Folding along the blue (*exo* angles) and magenta edges (*endo* angles) generates the two polyhedra. A unit cell of the 2D lattice is highlighted (green edges). The position of the symmetry axes of the plane lattice and those of the resulting polyhedra are shown with black symbols. The lattice points that become identical upon folding are labelled with the same letter. (**b**) Transformation of the symmetry axes upon folding. Axes of the plane lattice that become icosahedral symmetry axes without changing their order are coloured black in the middle and right pictures. Axes that become icosahedral symmetry axes of a different order are coloured purple. Axes that become local symmetry axes are coloured orange.

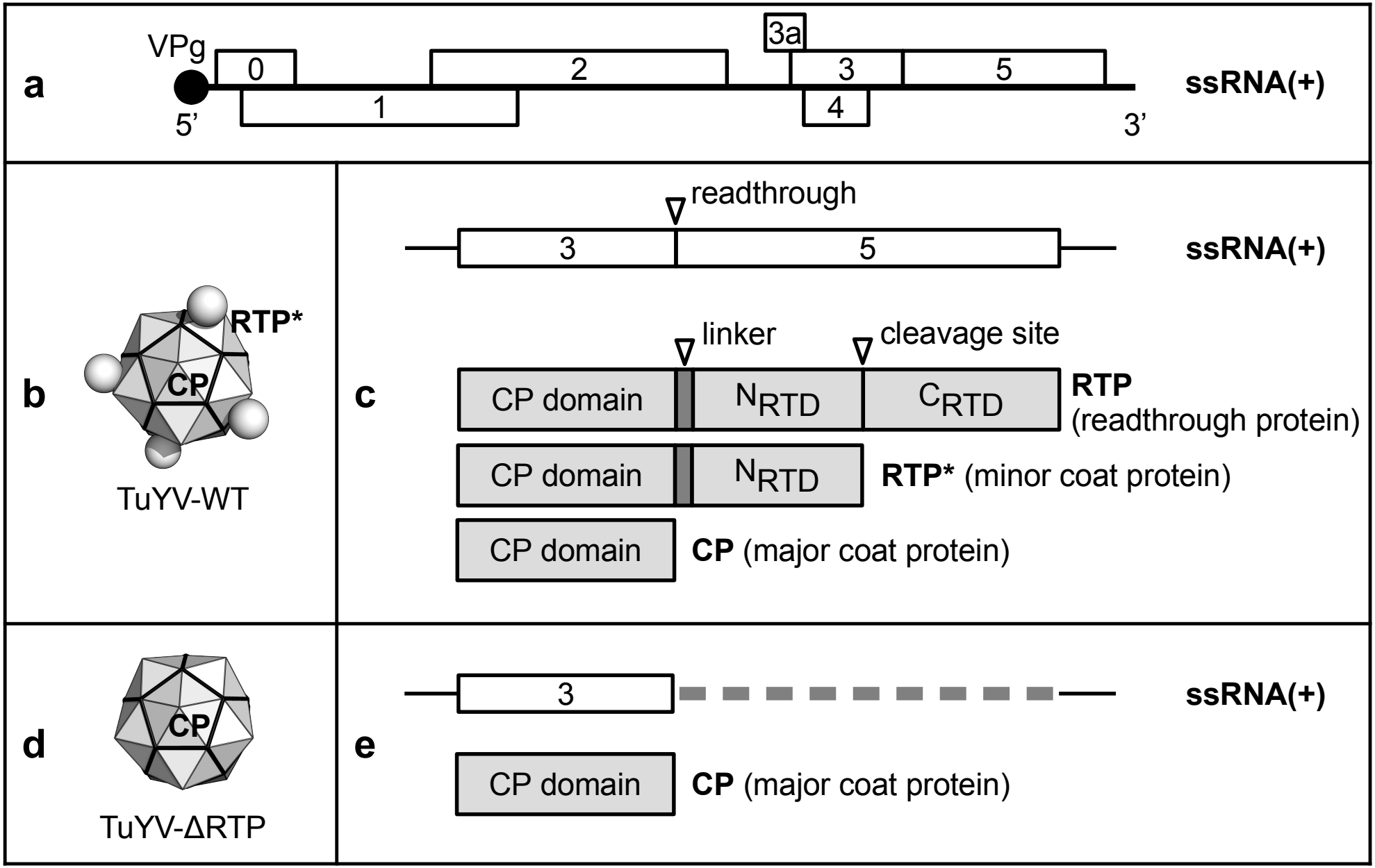
a
VPg
5'
0
1
2
3a
3
4
5
3'
ssRNA(+)
b
RTP*
CP
TuYV-WT
c
readthrough
3
5
ssRNA(+)
linker
cleavage site
CP domain
N RTD
C RTD
RTP
(readthrough protein)
CP domain
N RTD
RTP* (minor coat protein)
CP domain
CP (major coat protein)
d
CP
TuYV-ΔRTP
e
3
ssRNA(+)
CP domain
CP (major coat protein)

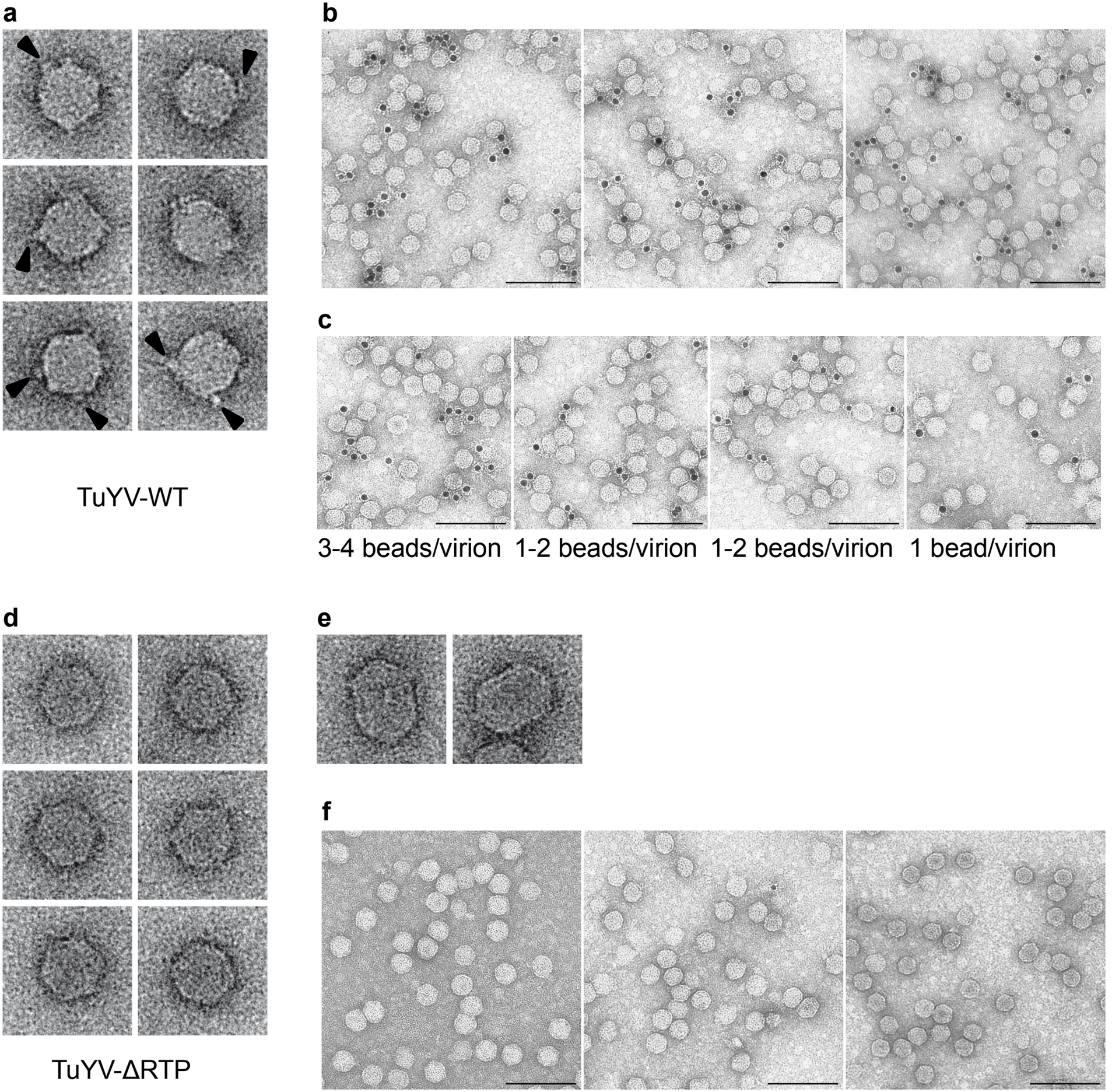
a
b
c
TuYV-WT
3-4 beads/virion
1-2 beads/virion
1-2 beads/virion
1 bead/virion
d
e
f
TuYV-ΔRTP

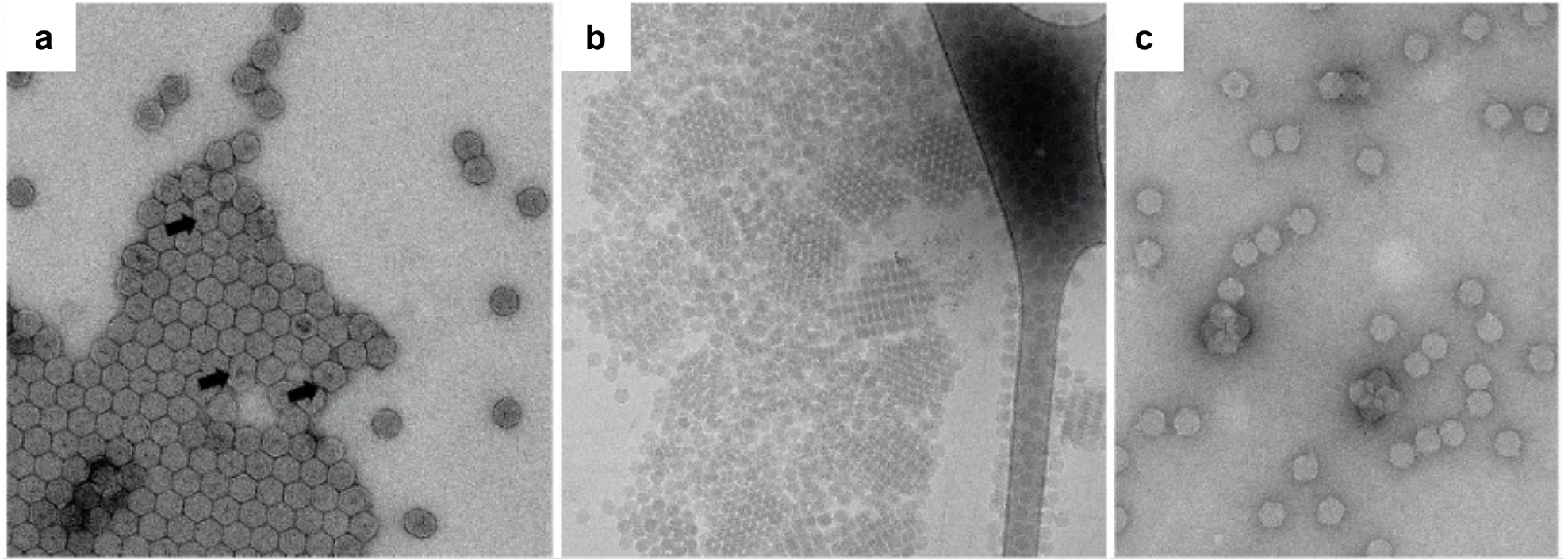
a
b
c

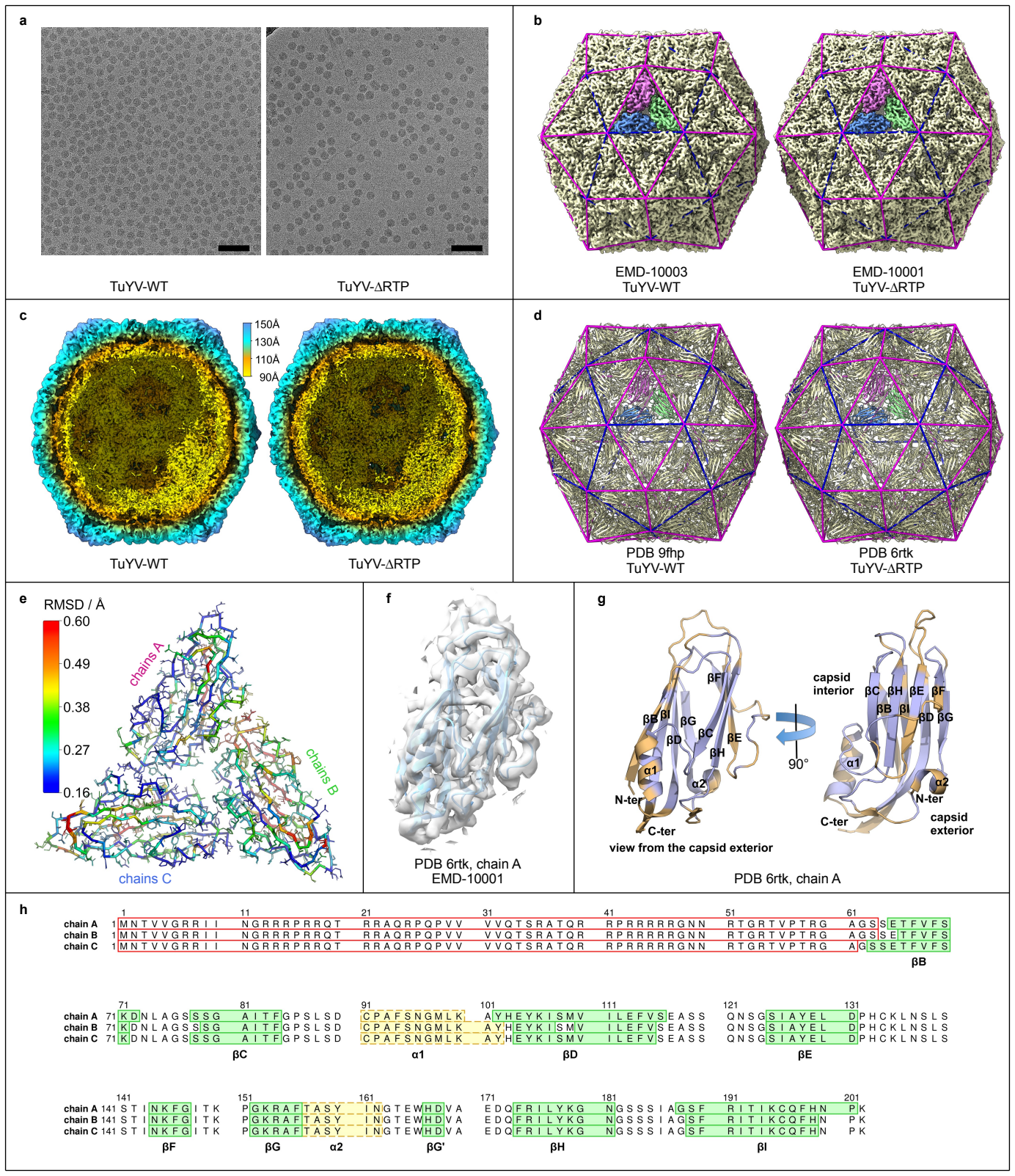
a
TuYV-WT
TuYV-ΔRTP
b
EMD-10003
TuYV-WT
EMD-10001
TuYV-ΔRTP
c
150Å
130Å
110Å
90Å
TuYV-WT
TuYV-ΔRTP
d
PDB 9fhp
TuYV-WT
PDB 6rtk
TuYV-ΔRTP
e
RMSD / Å
0.60
0.49
0.38
0.27
0.16
chains A
chains B
chains C
f
PDB 6rtk, chain A
EMD-10001
g
βF
βB βI
βG
βD
βC
βE
βH
α1
α2
N-ter
C-ter
view from the capsid exterior
90°
capsid interior
βC βH βE βF
βB βI βD βG
α1
α2
N-ter
C-ter
capsid exterior
PDB 6rtk, chain A
h
chain A 1 MNTVVGRRII NGRRRPRRQT RRAQRPQPVV VVQTSRATQR RPRRRRRGNN RTGRTVPTRG AGSSETFVFS
chain B 1 MNTVVGRRII NGRRRPRRQT RRAQRPQPVV VVQTSRATQR RPRRRRRGNN RTGRTVPTRG AGSSETFVFS
chain C 1 MNTVVGRRII NGRRRPRRQT RRAQRPQPVV VVQTSRATQR RPRRRRRGNN RTGRTVPTRG AGSSETFVFS
βB
chain A 71 KDNLAGSSSG AITFGPSLSD CPAFSNGMLK AYHEYKISMV ILEFVSEASS QNSGSIAYEL DPHCKLNSLS
chain B 71 KDNLAGSSSG AITFGPSLSD CPAFSNGMLK AYHEYKISMV ILEFVSEASS QNSGSIAYEL DPHCKLNSLS
chain C 71 KDNLAGSSSG AITFGPSLSD CPAFSNGMLK AYHEYKISMV ILEFVSEASS QNSGSIAYEL DPHCKLNSLS
βC α1 βD βE
chain A 141 STINKFGITK PGKRAFTASY INGTEWHDVA EDQFRILYKG NGSSSIAGSF RITIKCQFHN PK
chain B 141 STINKFGITK PGKRAFTASY INGTEWHDVA EDQFRILYKG NGSSSIAGSF RITIKCQFHN PK
chain C 141 STINKFGITK PGKRAFTASY INGTEWHDVA EDQFRILYKG NGSSSIAGSF RITIKCQFHN PK
βF βG α2 βG' βH βI

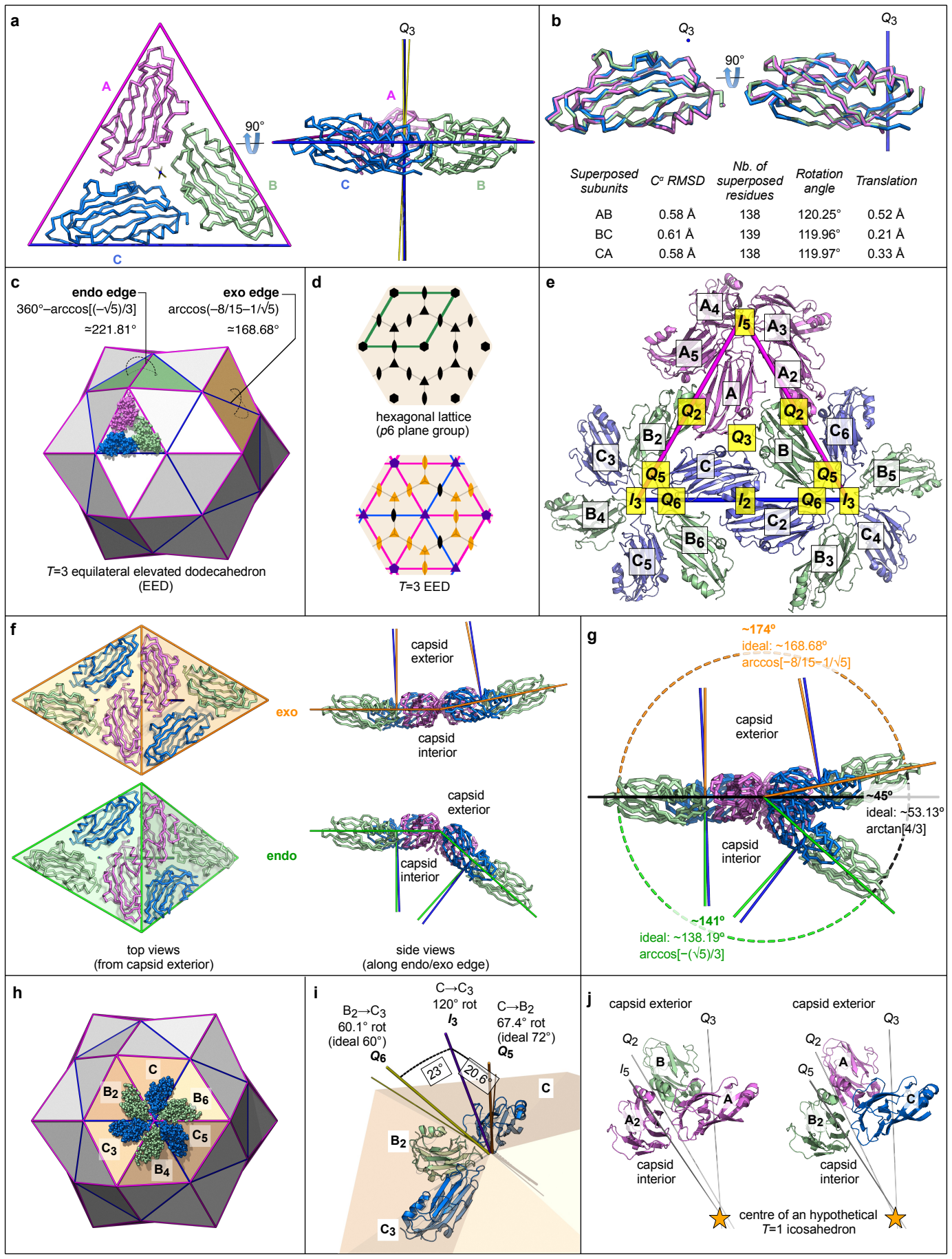
a
A
B
C
90°
Q3
b
90°
Superposed subunits
Cα RMSD
Nb. of superposed residues
Rotation angle
Translation
AB 0.58 Å 138 120.25° 0.52 Å
BC 0.61 Å 139 119.96° 0.21 Å
CA 0.58 Å 138 119.97° 0.33 Å
c
endo edge
360°–arccos[(–√5)/3]
≈221.81°
exo edge
arccos(–8/15–1/√5)
≈168.68°
T=3 equilateral elevated dodecahedron (EED)
d
hexagonal lattice (p6 plane group)
T=3 EED
e
A4
I5
A3
A5
A2
A
Q2
Q3
B
B2
C6
C3
C
Q5
B5
I3
Q6
I2
B4
C2
C4
B6
C5
B3
f
exo
endo
capsid exterior
capsid interior
top views (from capsid exterior)
side views (along endo/exo edge)
g
~174°
ideal: ~168.68°
arccos[−8/15−1/√5]
capsid exterior
~45°
ideal: ~53.13°
arctan[4/3]
capsid interior
~141°
ideal: ~138.19°
arccos[−(√5)/3]
h
C
B2
B6
C5
C3
B4
i
B2→C3
60.1° rot
(ideal 60°)
Q6
C→C3
120° rot
I3
C→B2
67.4° rot
(ideal 72°)
Q5
23°
20.6°
C
B2
C3
j
capsid exterior
Q3
Q2
B
I5
A
A2
capsid interior
Q5
C
centre of an hypothetical T=1 icosahedron

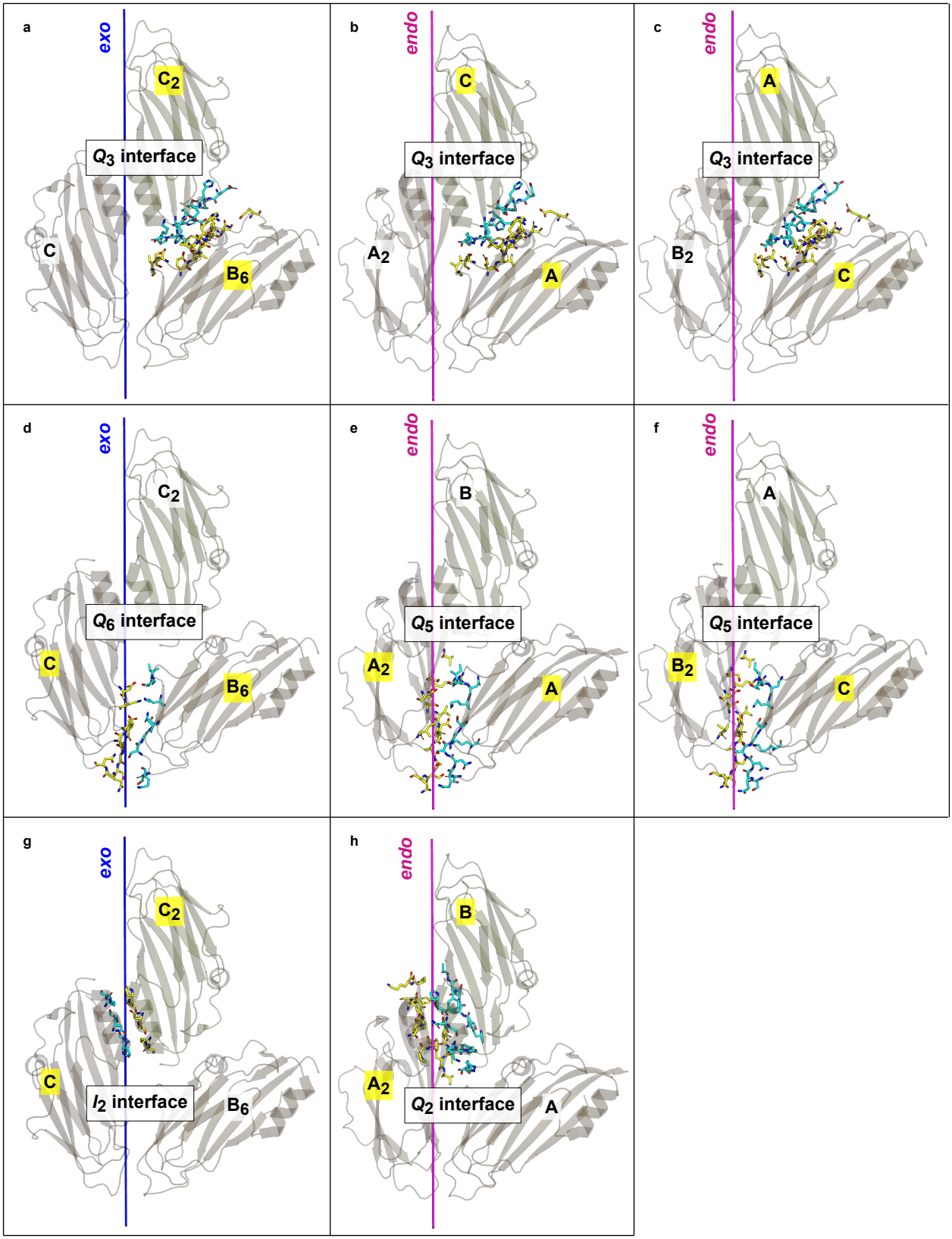
a
exo
C2
Q3 interface
C
B6
b
endo
C
Q3 interface
A2
A
c
endo
A
Q3 interface
B2
C
d
exo
C2
Q6 interface
C
B6
e
endo
B
Q5 interface
A2
A
f
endo
A
Q5 interface
B2
C
g
exo
C2
C
I2 interface
B6
h
endo
B
A2
Q2 interface
A

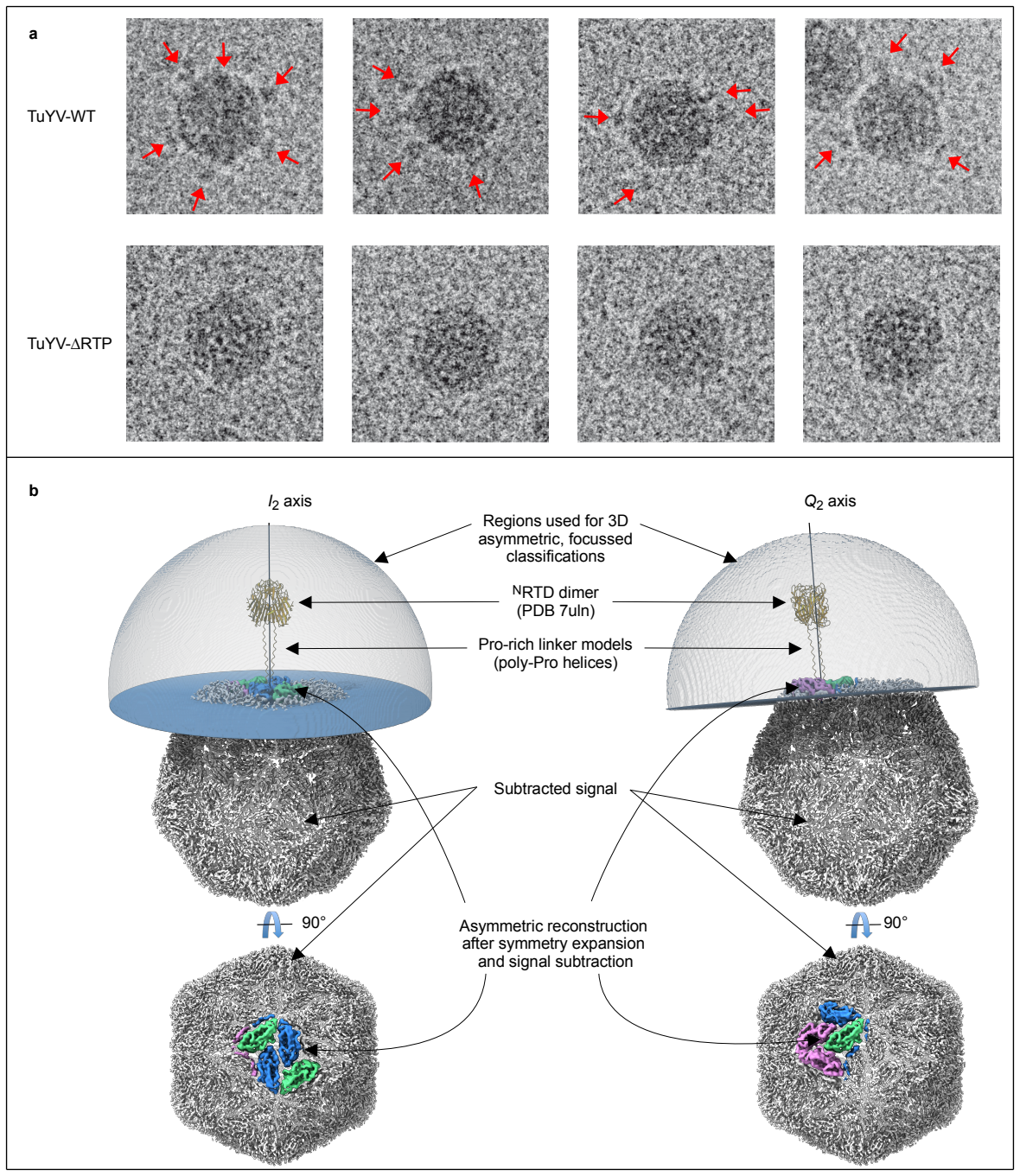
a
TuYV-WT
TuYV-ΔRTP
b
I_2 axis
Q_2 axis
Regions used for 3D asymmetric, focussed classifications
^{N}RTD dimer (PDB 7uln)
Pro-rich linker models (poly-Pro helices)
Subtracted signal
90°
90°
Asymmetric reconstruction after symmetry expansion and signal subtraction